Crystalline Gibbs Monolayers of DNA-Capped Nanoparticles at the Air–Liquid Interface

Michael J. Campolongo,[†] Shawn J. Tan,[†] Detlef-M. Smilgies,[‡] Mervin Zhao,[§] Yi Chen,[⊥] Iva Xhangolli,[∥] Wenlong Cheng,[⊥,*] and Dan Luo[∥,*]

[†]Department of Biomedical Engineering, Cornell University, Ithaca, New York 14853, United States , [‡]Cornell High Energy Synchrotron Source, Cornell University, Ithaca, New York 14853, United States , [§]Department of Chemistry, Cornell University, Ithaca, New York 14853, United States , [⊥]Department of Chemical Engineering, Monash University, Clayton, Victoria 3150, Australia, and [∥]Department of Biological and Environmental Engineering, Cornell University, Ithaca, New York 14853, United States

ABSTRACT Using grazing-incidence small-angle X-ray scattering in a special configuration (parallel SAXS, or parSAXS), we mapped the crystallization of DNA-capped nanoparticles across a sessile droplet, revealing the formation of crystalline Gibbs monolayers of DNA-capped nanoparticles at the air–liquid interface. We showed that the spatial crystallization can be regulated by adjusting both ionic strength and DNA sequence length and that a modified form of the Daoud–Cotton model could describe and predict the resulting changes in interparticle spacing. Gibbs monolayers at the air–liquid interface provide an ideal platform for the formation and study of equilibrium nanostructures and may afford exciting routes toward the design of programmable 2D plasmonic materials and metamaterials.

KEYWORDS: DNA-capped nanoparticles · superlattices · Gibbs monolayers · synchrotron radiation · GISAXS

The assembly of nanoparticles into highly ordered arrays (superlattices) has opened an exciting new avenue toward the realization of metamaterials and nanodevices.[1−8] To obtain nanoparticle superlattices, two distinct approaches have been demonstrated:[9] (1) DNA-programmable crystallization in solution[10−13] and (2) drying-mediated nanoparticle crystallization on solid or liquid interfaces.[1−8,14−19] The former approach takes advantage of the unique Watson–Crick base-pairing of DNA to program interparticle forces (enthalpic effects); the latter achieves superlattices by optimizing like-charge repulsion or steric hindrance during solvent evaporation (entropic effects). Notably, each approach alone suffers limitations. The DNA-programmable approach has been able to form only stable ordered structures in solution, a potential problem for solid-state device integration. The drying-mediated approach typically relies on alkyl molecule spacers, ultimately restraining the structural and functional properties due to synthetic limitations on longer molecular ligand length.

Recently, we have combined the aforementioned strategies by using DNA as a "dry ligand" under unusually low ionic strength and successfully obtained 2D and 3D nanoparticle superlattices in the dehydrated state.[20−23] The highly extendable and controllable molecular lengths of DNA ligands enable tailoring of both structural (interparticle spacing) and functional properties (plasmonic and mechanical) over a wide window. In particular, the edge-to-edge interparticle spacing for DNA-based monolayer superlattice sheets can be adjusted up to 20 nm,[21] which is a significantly wider range than has been achieved with alkyl ligands.[24] More importantly, such superlattices are highly customizable into single-particle-width corrals,[20] single-particle-thickness superlattice discs,[20] and free-standing superlattice membranes.[21] Thus, our strategy may constitute a promising step to enable the integration of bioinspired superlattices into solid-state nanodevices.

DNA-capped nanoparticles provide an ideal testing system for exploring nanoscale self-assembly. Recent research efforts by several groups including ours have employed synchrotron radiation to reveal the nature of such interactions. For example, Gang and Mirkin have each reported temperature-dependent nanoparticle crystallization in bulk buffered solutions.[10,11] In parallel, our group has revealed the crystallization dynamics of DNA-capped nanoparticles in real-time using a drying-mediated self-assembly process.[22] While these previous studies utilized transmission small-angle X-ray scattering (SAXS) to uncover temperature dependence and temporal dynamics of 3D nanoparticle crystallization,

* Address correspondence to wenlong.cheng@monash.edu, dl79@cornell.edu.

Received for review June 28, 2011 and accepted September 3, 2011.

Published online September 03, 2011
10.1021/nn202383b

here we utilized a technique we termed parallel SAXS (parSAXS) to reveal spatial crystallization events of DNA-capped nanoparticles over a microliter-scale droplet. Notably, we observed 2D nanoparticle crystallization into Gibbs monolayers at the air–liquid interface. In contrast with crystalline monolayers formed upon drying,[21] these Gibbs assemblies are in dynamic equilibrium with the bulk solution and can be obtained under high-salt conditions.

While extensive studies have been performed on amphiphilic or hydrophobic ligand-capped nanoparticles assembled into Langmuir layers,[1,25−27] the interfacial assembly of hydrophilic nanoparticles in aqueous solvent into Gibbs layers is not well understood. Unlike a Langmuir layer, a Gibbs layer is an equilibrium system in which surface coverage is driven by the solute concentration and is independent of solvent volume.[28,29] In the case of DNA-capped nanoparticles, base-pairing and the charge of the DNA ligands provide additional parameters for controlling the assembly of Gibbs layers. Our results revealed the formation of crystalline Gibbs monolayers at the air–liquid interface under optimized ionic strengths. Furthermore, the effect of ionic strength on interparticle spacing could be described by a modified form of the Daoud–Cotton model.[30]

RESULTS AND DISCUSSION

In this work, we investigated the spatial DNA-mediated crystallization process across a sessile drop using transmission SAXS in a raster scanning mode. We studied the interparticle interactions by varying spacer length, concentration, and ionic strength to understand their roles in mediating the interactions between particles. All single-stranded DNA (ssDNA) used in our system were comprised of a polythymine spacer with variable length and a palindromic base-pairing region (5′-SH-C_6-$(dT)_N$-CTCATGAG, where N = 7, 15, or 30), as shown in Figure 1a. This base-pairing region was necessary to facilitate rapid crystallization of DNA-capped nanoparticles, as demonstrated by our previous work.[22] We developed a "lab-on-a-drop" technique in which a microliter-scale drop of solution was placed on a clean silicon wafer, which is particularly useful for when sample quantity is limited. In a typical experiment, a 1.5 μL droplet of DNA-capped gold nanoparticles was placed on a cleaned silicon substrate on a sample stage such that the plane of the substrate was parallel to the incident beam (Figure 1b). The parSAXS configuration is a special case of grazing-incidence SAXS (GISAXS) in which the angle of incidence is 0°. Notably, parSAXS is uniquely capable of observing interfacial phenomena while avoiding scattering effects that result from X-ray reflection off of the supporting substrate. As the beam skimmed the apex of the droplet, the scattering cross section resulted

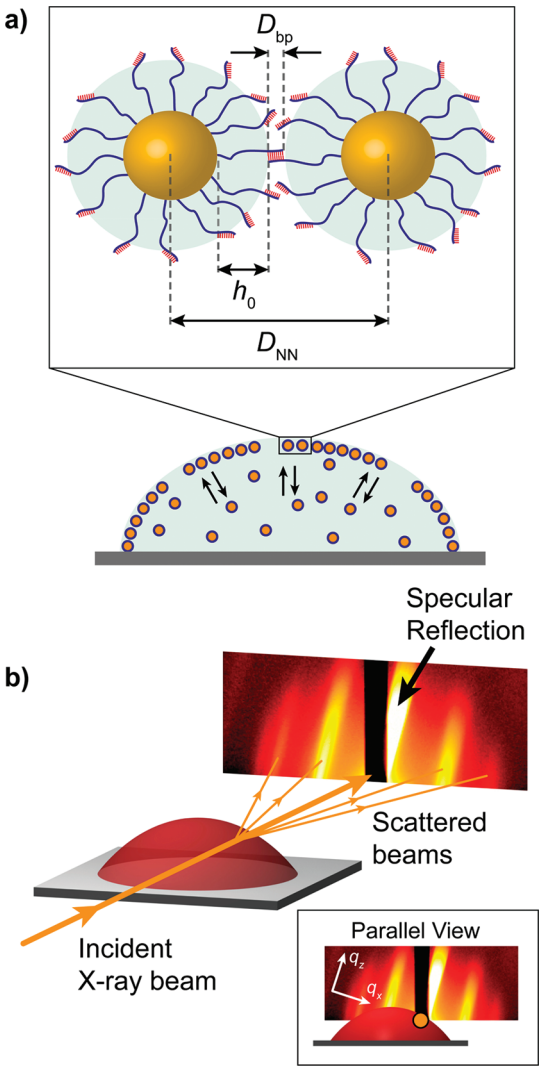

Figure 1. (a) Schematic illustrating how nanoparticles are distributed in the Gibbs system. We model the nanoparticle spacing as a sum of flexible corona heights and the length of the rigid hybridized region. (b) Experimental setup of parSAXS experiments. The DNA-NP droplet is placed on a cleaned Si substrate within a sealed chamber. The sample stage is positioned such that the X-ray beam passes through the droplet parallel to the plane of the substrate. The specular reflection due to the incident beam is indicated and is not included in the subsequent analysis. We define the coordinate system of the scattering vector such that q_z is parallel to the specular reflection of the incident beam off of the droplet surface and q_x is perpendicular to q_z and thus parallel to the local surface segment.

from the air–liquid interface, providing information about the air–liquid interface directly. When the relative beam position was decreased in the z-direction, the beam passed through less of the interface and the scattering signal was instead dominated by mobile particles dissolved in the bulk, as well as precipitates when in close proximity to the substrate.

In order to minimize solvent evaporation, the sample droplet was housed in a sealed chamber containing a reservoir filled with a sodium chloride solution of the same concentration as the droplet, thus maintaining a

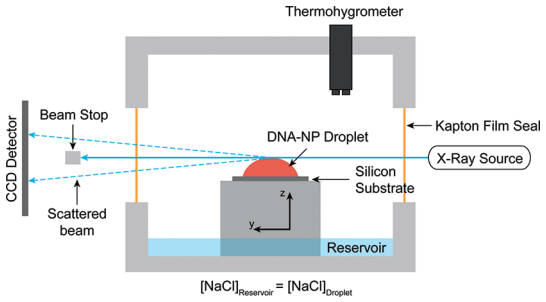

Figure 2. Schematic diagram of the experimental setup. A droplet of DNA-capped nanoparticle solution with a well-defined volume is placed onto a clean silicon wafer. The droplet volume can be stabilized by using a salt solution of the same concentration in the reservoir to control the vapor pressure inside the closed chamber. In order to dynamically control the concentration inside the droplet, the water vapor concentration in the chamber can be reduced by flowing dry helium gas through the cell. A thermohygrometer monitors temperature and relative humidity in the chamber.

similar vapor pressure (Figure 2). A raster scan of the droplet obtained by incrementally stepping the sample stage in the *x* and *y* directions provided valuable information regarding the state of the nanoparticles. In particular, streaks that were observed perpendicular to the air−liquid interface were indicative of nanoparticle monolayers, analogous to GISAXS measurements of both ordered and amorphous FePt nanocrystal monolayers on silicon.[31] Multiple parallel streaks arise from scattering off of a two-dimensional monolayer with long-range order, while a single continuous streak indicates short-range order only (Figure S2, Supporting Information). On the other hand, a ring pattern indicates the formation of a three-dimensional aggregate with short-range order. In some instances, a composite spectra can result from simultaneous scattering off of both a crystalline monolayer and an aggregate due to the finite size of the beam, as shown in Figure 3. The diffuse background in the spectra obtained from the droplet interior corresponded to dilute scattering from freely dispersed nanoparticles in solution (Figure S1, Supporting Information). Although monolayers were observed over a wide range of salt concentrations, ordered monolayers were observed only over a narrower range of salt concentrations, particularly at the droplet apex. A parSAXS spectrum obtained close to the droplet apex is shown in Figure 2. Notably, up to fifth-order peaks were observed, which are indicative of well-defined crystalline monolayers (Figure 3). The Bragg diffraction pattern consists of parallel lines in which the angle with the horizontal corresponds to the normal of the droplet. This is true of any spectra measured along the droplet edge, suggesting flexible crystalline formations dependent on the droplet curvature.

By varying the salt concentration in the colloidal droplet, we observed that the formation of Gibbs nanoparticle monolayers at the air−liquid interface

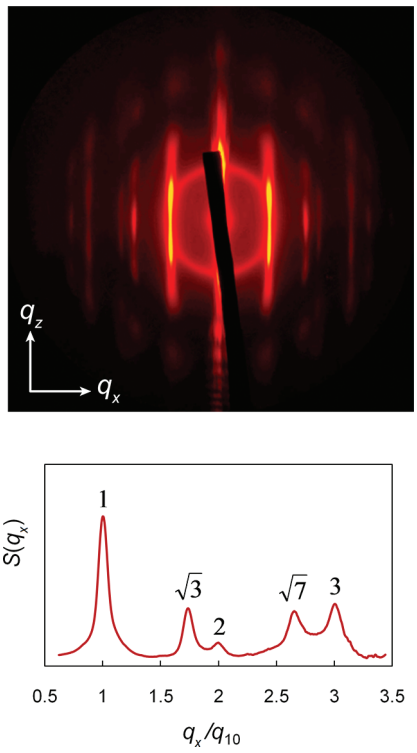

Figure 3. Example spectrum showing a high degree of crystalline order (*N* = 7, [NaCl] = 500 mM). The relative positions of the Bragg peaks with respect to the first-order peak indicate a simple hexagonal lattice.

occurred within a range of salt concentrations. Figure 4 shows the formation of Gibbs layers at the droplet apex over a salt concentration range of 100 to 1000 mM. Below 100 mM NaCl, only the form factor was observed, likely due to strong electrostatic repulsion between poorly screened nanoparticles, which prevented accumulation at the air−liquid interface. Above 750 mM NaCl, streak-like scattering patterns disappeared and only a faint ring-like pattern was present, suggesting the formation of a precipitate. Both short-range ordered and crystalline monolayers formed between 100 and 750 mM NaCl. At 500 mM, crystalline order was optimal in terms of peak width and intensity of higher order scattering peaks (up to third-order).

The crystalline order was modeled using a static Debye−Waller factor, σ_{DW} (see Supporting Information),[32] which was fit to the experimental form factor using grain size diameter, D_g, and σ_{DW} as fitting parameters. In this model, the grain size is inversely proportional to the widths of the Bragg peaks in the one-dimensional spectra. The static Debye−Waller factor is of the form $D(q_x) = \exp(-\sigma_{DW}^2 q_x^2)$ and accounts for local deviations of individual nanoparticles from perfect crystalline order. Higher order Bragg reflections are more sensitive to local disorder, and their intensities diminish very quickly with increasing σ_{DW}. After correcting for resolution effects,[33] a fit of the 500 mM NaCl spectra from Figure 4 yielded D_g = 365 nm and σ_{DW} = 2.87 nm, which were the optimal

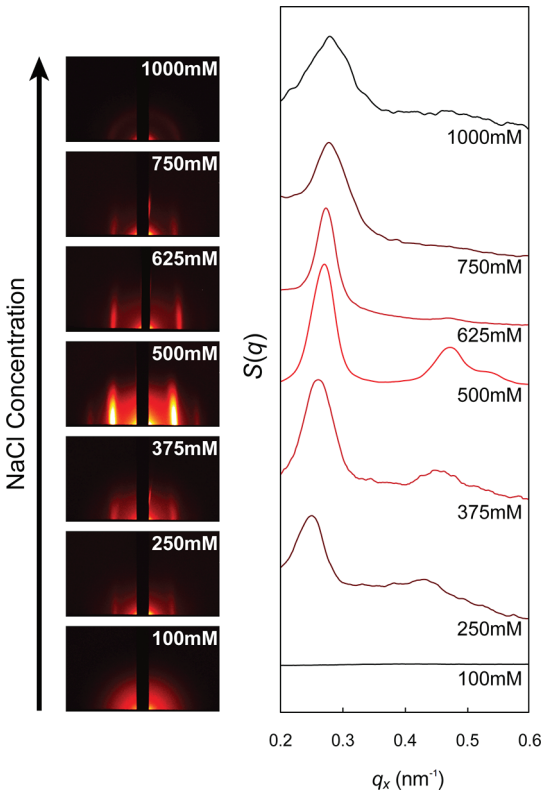

Figure 4. Effects of ionic strength on monolayer formation for a 15-base spacer. Monolayers are observable at the droplet apex from 250 to 750 mM and are crystalline at 500 mM. At 100 mM, only form factor scattering is observed, so at best there is a dilute monolayer without short-range order. At 1000 mM, only short-range order remains. The experimental form factor was removed from each one-dimensional spectra.

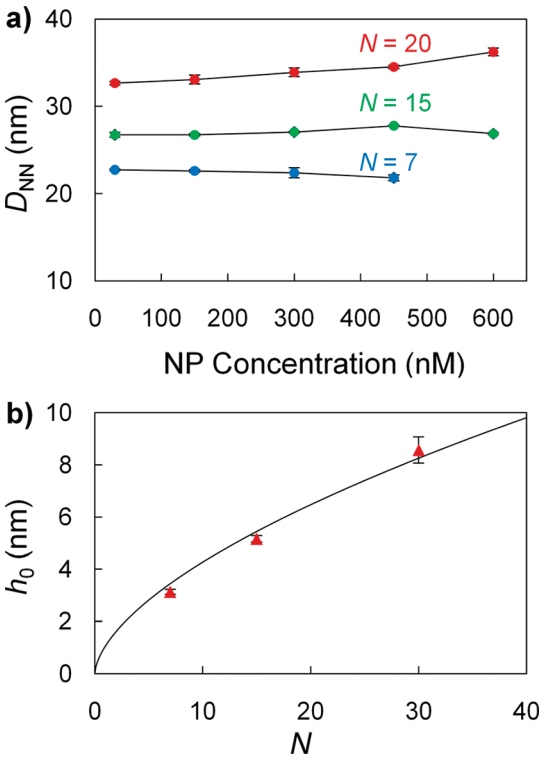

Figure 5. The corona height was computed from the average interparticle spacing at three separate locations along the air–liquid interface of an individual colloidal droplet. The small variation, as indicated by the error bars, suggests that the interparticle spacing was fairly uniform along the droplet profile and that the effect of the air–liquid–substrate meniscus was negligible. (a) Nearest neighbor spacing was not significantly affected by changes in nanoparticle concentration. (b) The corona height at constant density is dependent only on spacer length and is consistent with that of an uncompressed corona as described by polymer brush theory.

values of any salt concentration obtained (Figures S3, S4 and Table S1, Supporting Information). These results indicate that, while Gibbs layers can be achieved over a range of salt concentrations, crystalline order is highly sensitive to ionic strength.

The interparticle forces in DNA-capped nanoparticle colloids are dominated by DNA–DNA interactions, rather than by the core–core interactions of gold nanoparticles. At 25 °C, k_bT = 25.6 meV, which is five times greater than the van der Waals attractive force between cores at the smallest spacing value of D_{NN}, V_{vdW}(22.1 nm) = 5.7 meV (see Supporting Information). Our analysis of interparticle spacing by varying both nanoparticle concentration and spacer length revealed that no compression occurred between the adjacent DNA coronas. In a Langmuir system, the monolayer will be compressed with increasing nanoparticle monolayer concentration, while in a Gibbs layer the surface density is controlled by the bulk concentration. However, it was found that varying the bulk concentration while holding the ionic strength constant did not result in any significant compression in terms of interparticle spacing and corona height (Figure 5a). This result indicates that the density in the Gibbs layer *per se* is too small to lead to crystallization. However, crystalline islands can be formed by virtue of Watson–Crick base-pairing.

We further demonstrated that the DNA corona height in our system can be modeled by polymer brush theory.[34] Figure 5b shows how the corona height varies with DNA spacer length. Previously, we used an entropic spring model to describe the compression between densely packed DNA-capped nanoparticles.[22] On the basis of this analysis, the corona height was modified with a compressive force term to account for deformation that might occur between nanoparticle coronas packed together at the interface (see Supporting Information). We would then expect the compressed corona height to scale as $h'_0 = aN^{3/5}\sigma^{1/5}R^{2/5} - (Nb^2F/3k_BT)$, where a is a proportionality constant, N is the number of DNA bases, σ is the DNA coating density, R is the nanoparticle radius, b is the Kuhn length, and F is the equilibrium compressive force acting on the corona. Assuming constant density and using a and F as fitting parameters (Figure 5b), the best fit was achieved using $F = 0$, which simplified to the equation

predicted by uncompressed brush theory. Furthermore, because the DNA corona height scales only with N, we can assume that the ligand density is independent of DNA length. This thermodynamic description of our system implies that the interparticle spacing of the Gibbs nanoparticle monolayers can be readily controlled simply by engineering the lengths of DNA spacers used to functionalize nanoparticles.

We next investigated the effects of ionic strength on the interparticle spacing within the monolayers. It was expected that higher concentrations of monovalent salt ions would decrease the interparticle spacing by screening, thus reducing intrastrand repulsive charges (Figure 6a). On the other hand, reducing the salt concentration would increase the intrastrand repulsion and consequently the interparticle spacing. This reversible behavior was previously observed in three-dimensional crystals as reported by Gang and coworkers.[35]

The effect of ionic strength on nearest neighbor spacing in the crystalline monolayers can be best described by the Daoud−Cotton model. We previously defined and characterized the nanoparticle corona softness $\chi = h_0/R$, which was used to model the corona compression after solvent evaporation.[22] We will then express the softness in terms of the Daoud−Cotton model[36,37] as

$$\chi = h_0/R = (1+kNbR^{-1}(\nu\sigma/L_K)^{1/3})^{3/5} - 1$$

where k is a proportionality constant typically taken as unity, N is the number of bases, b is the length per base (0.65 nm/base for ssDNA), σ is the surface density of polyelectrolyte chains, ν is the excluded volume parameter, and L_K is the Kuhn length. As proposed by Guo and Ballauff,[30] modifications may need to be made to this model in order to have quantitative agreement with experimental data. Thus, we will apply the theory of Argillier and Tirrell,[38] which approximates the excluded volume as $\nu \approx L_K^3$. Furthermore, Barrat and Joanny[39] showed that the persistence length varies linearly with the Debye screening length, $L_K \approx \kappa^{-1}$, for flexible polyelectrolytes. The Debye screening length for water at 25 °C is given by $\kappa^{-1} = 1/(8\pi N_A L_B I)^{1/2}$, where I is the ionic strength (mol/m^3) and L_B is the Bjerrum length (0.714 nm), which simplifies to $\kappa^{-1}(\text{nm}) = 0.304C^{-1/2}$ for added concentrations, C (mol/L), of NaCl. By applying these two arguments, the corona height will scale as $h_0 \approx C^{-2/5}$ when R is small. The corona height can now be expressed as

$$h_0/R = (1+kN_{eff}bR^{-1}(\sigma/\kappa^2)^{1/3})^{3/5} - 1$$

after making the appropriate substitutions and allowing the constant k to absorb any additional multiplicative constants. We also modified the expression with $N_{eff} = N + N_0$, where N_0 is an empirical additive term to account for an effective increase in the spacer segment. This increase can be attributed to limited conformational freedom of the single-stranded spacer in the vicinity of the more densely charged hybridization region,[40] as well as to the contribution from single-stranded regions that are only partially hybridized. An estimate of $k \approx 2.7$ can be made from the parameters reported by Gang and co-workers[41] (h_0 = 8 nm, R = 6 nm, N = 30, b = 0.65 nm/base, σ = 0.145 chains/nm^2, C_a = 0.3 M). Using σ and N_0 as the only adjustable parameters (based on a constant oligonucleotide density, as discussed above), we observe in Figure 6b an excellent fit of the model to our experimental data for the three different ligands, which yielded N_0 = 2.45 and σ = 0.17 chains/nm^2 for all three nanoparticle systems. The oligonucleotide footprint was σ^{-1} = 5.88 nm^2 for when R = 6.8 nm, which compares reasonably well with the experimentally measured footprint of 6.0 ± 1 nm^2 for nanoparticles in which R = 7.5 nm.[42] This model shows the relative importance of the parameters that regulate interparticle spacing and could easily be extended to 3D crystals. Increasing the ionic strength effectively decreases the persistence length of the ssDNA spacers. Consequently, this is an important consideration in the design of DNA nanostructures, particularly those that exploit the flexibility of ssDNA components under various buffer conditions and local environments.

We further demonstrated that the formation of crystalline nanoparticle monolayers were controllable by dynamically varying the ionic strength *via* evaporation and rehydration of the colloidal droplet (Figure 7). For this experiment, we used pure water in the sample cell reservoir, which caused diffusive transport of water through the vapor phase to the droplet due to its salt concentration. In order to dry the droplet, dry helium gas was flown through the cell to dilute the water vapor content in the cell. The helium flow was then stopped and the droplet swelled again. Since the particle and salt content within the droplet are fixed, water vapor uptake and evaporation caused both particle and salt concentrations to vary according to the water content in the drop.

Crystalline monolayers were obtained by evaporating the droplet to 25% of the original volume (Figure S5, Supporting Information), resulting in a 4-fold increase in salt and nanoparticle concentration. These monolayers were maintained upon rehydration of the droplet. While the nanoparticle concentration also increased upon evaporation, it did not seem to play a significant role in monolayer formation as described earlier. However, if the droplet was evaporated such that the salt concentration exceeded the crystallization threshold, the nanoparticles precipitated out, and thus no monolayers were observed when the droplet recovered to its original volume. These results were in

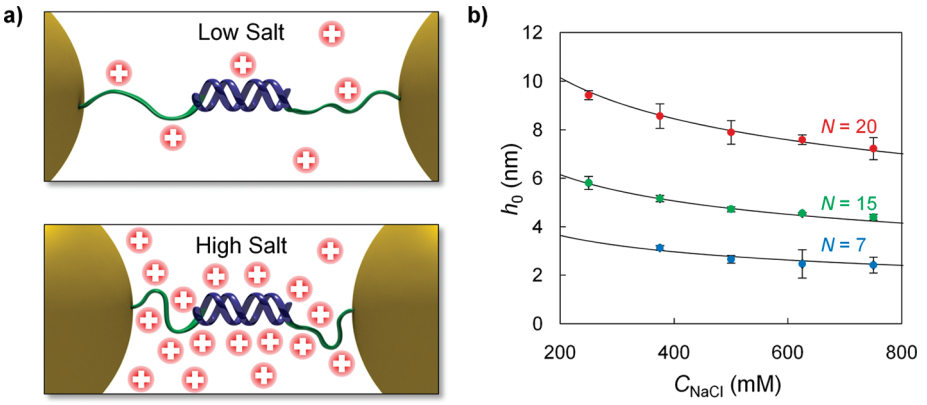

Figure 6. (a) Positive counterions can screen negative repulsive charges between DNA strands to reduce the interparticle spacing. Only one strand per particle is shown for illustrative purposes. (b) Fit of the Daoud–Cotton model to brush height *versus* salt concentration for droplets containing nanoparticles with different spacer lengths.

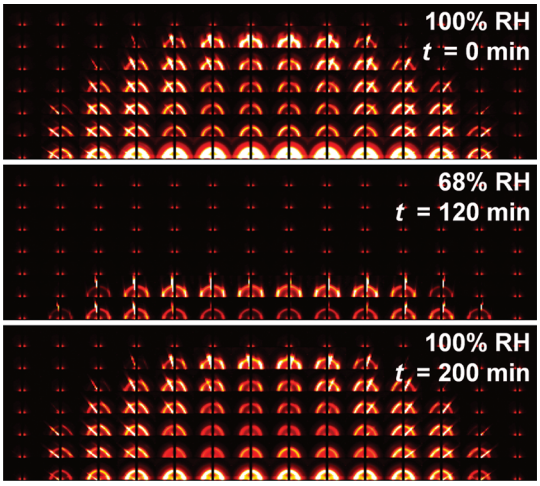

Figure 7. parSAXS raster scans of a nanoparticle droplet kept in a chamber with variable humidity (N = 7, [NaCl] = 1000 mM). (a) At 100% relative humidity (RH), the droplet grew slowly *via* water vapor uptake due to the salt concentration in the droplet. (b) At 68% RH the droplet was almost dried after 2 h. (c) Back at 100% RH for an additional 80 min the drop regained its former shape.

agreement with our previously report on the cycling phenomena of interparticle spacing in nanoparticle colloidal droplets,[22] which is attributed to volume-driven changes in ionic strength.

CONCLUSION

In summary, spatial mapping of a solution droplet profile with parSAXS revealed the formation of Gibbs monolayers of DNA-capped nanoparticles at the air–liquid interface. Crystalline and short-range ordered monolayers of nanoparticles were obtained depending on the ionic strength of the solution. The change in interparticle spacing for different salt concentrations was shown to be described by our modified form of the Daoud–Cotton model. Our findings reveal that DNA-programmability is not limited to bulk solution but is extendable to the air–liquid interface. Due to its dynamic nature with particles freely exchanging between bulk and surface reservoirs, the air–liquid interface provides a unique lab-on-a-drop platform for the preparation of equilibrium nanostructures. The ability to control spatial crystallization of biofunctionalized nanoparticles, particularly at 2D interfaces, may open up exciting routes to design programmable 2D plasmonic materials, facilitating the integration of bioderived wet structures into dried solid-state devices.

METHODS

Nanoparticle Preparation. Gold nanoparticles with diameters of ~14 nm were synthesized according to the literature.[14,43] Thiolated oligonucleotides (Integrated DNA Technologies, Inc.) were deprotected using dithiothreitol and incubated with nanoparticle solutions at a DNA-to-nanoparticle ratio of 1000:1. Charge screening was performed by adding sodium chloride at 30 min intervals to a final concentration of 0.3 M to generate densely capped nanoparticles. The mixture was aged at room temperature for another 10–12 h and centrifuged and exchanged in Milli-Q water.

X-ray Scattering Experiments. Most parSAXS experiments were performed at the D1 station at the Cornell High Energy Synchrotron Source (CHESS). The D1 station receives a high-flux X-ray beam (typically 10^{12} photons s^{-1} mm^{-2}) with a wavelength of 1.22 Å at a bandwidth of 1.5% using a multilayer monochromator. A MedOptics CCD detector was used to capture the scattered images at a beam energy of 10 keV and with a beam size of 0.3 mm (H) × 0.2 mm (V). Some parSAXS images were also obtained at the SAXS/WAXS beamline of the Australian Synchrotron. A 1.5 μL droplet of DNA-capped nanoparticles was placed on a cleaned silicon substrate on the sample stage, which was oriented parallel to the incident beam. The sample was housed in a closed chamber containing a reservoir filled with a NaCl solution of the same concentration as the droplet to maintain a similar vapor pressure to minimize evaporation effects (see Supporting Information).

Data Processing. The nanoparticle size distribution was measured to be 13.6 ± 0.7 nm by fitting the experimental form factor obtained from bulk scattering at the center of the droplet

to

$$F(q) = \int_0^\infty N(R)\, P(q,R) R^6\, dR$$

where

$$P(q,R) = (3[\sin(qr) - qR\cos(qR)]/(qR)^3)^2$$

for spherical nanoparticles of radius R, and

$$N(R) = \exp[-(R - R_0)^2/(2\sigma^2)]/\sqrt{2\pi\sigma^2}$$

assuming a Gaussian size distribution with a mean radius R_0 and standard deviation σ.

Scattering patterns from Gibbs layers result from a product of the form factor and structure factor.[31] The structure factor, $S(q_x)$, was obtained by extracting the experimental form factor, $F(q)$, obtained by a scan taken away from the droplet edge (Figure 3). For a two-dimensional hexagonal lattice, the nearest neighbor spacing for a given set of Miller indices (hk) can be determined from $D_{NN} = 4\pi(h^2 + hk + k^2)^{1/2}/(q(\sqrt{3}))$. Based on the schematic in Figure 1a, the corona height, h_0, can be expressed as $h_0 = (D_{NN} - 2R - L_{BP} - 2L_{6C})/2$, where $L_{BP} = 2.72$ nm (8 bases at 0.34 nm/base) and $L_{6C} = 0.5$ nm for the alkyl spacers.

Acknowledgment. We thank A. Gray-Weale for insightful discussions. M.J.C. is supported by the IGERT Program of the National Science Foundation under Agreement No. DGE-0654112, administered by the Nanobiotechnology Center at Cornell University. S.J.T. is a recipient of the National Science Scholarship awarded by the Agency for Science, Technology and Research, Singapore (A-STAR). W.L.C. acknowledges the New Staff Member Research Fund (2437404) in Faculty of Engineering, Monash University. D.L. acknowledges financial support from NYSTAR and an NSF CAREER award (grant no. 0547330). This work is based upon research conducted at the Cornell High Energy Synchrotron Source (CHESS), which is supported by the National Science Foundation and the National Institutes of Health/National Institute of General Medical Sciences under NSF award DMR-0936384. We also acknowledge the SAXS/WAXS beamline at the Australian Synchrotron for providing beam time.

Supporting Information Available: Additional details regarding the experimental setup, modeling, and mathematical derivations. This material is available free of charge *via* the Internet at http://pubs.acs.org.

REFERENCES AND NOTES

1. Collier, C. P.; Saykally, R. J.; Shiang, J. J.; Henrichs, S. E.; Heath, J. R. Reversible Tuning of Silver Quantum Dot Monolayers through the Metal-Insulator Transition. *Science* **1997**, *277*, 1978–1981.
2. Shevchenko, E. V.; Talapin, D. V.; Kotov, N. A.; O'Brien, S.; Murray, C. B. Structural Diversity in Binary Nanoparticle Superlattices. *Nature* **2006**, *439*, 55–59.
3. Pileni, M.-P. Self-Assembly of Inorganic Nanocrystals: Fabrication and Collective Intrinsic Properties. *Acc. Chem. Res.* **2007**, *40*, 685–693.
4. Talapin, D. V.; Shevchenko, E. V.; Bodnarchuk, M. I.; Ye, X.; Chen, J.; Murray, C. B. Quasicrystalline Order in Self-Assembled Binary Nanoparticle Superlattices. *Nature* **2009**, *461*, 964–967.
5. Xu, K.; Qin, L.; Heath, J. R. The Crossover from Two Dimensions to One Dimension in Granular Electronic Materials. *Nat. Nanotechnol.* **2009**, *4*, 368–372.
6. Dong, A.; Chen, J.; Vora, P. M.; Kikkawa, J. M.; Murray, C. B. Binary Nanocrystal Superlattice Membranes Self-Assembled at the Liquid-Air Interface. *Nature* **2010**, *466*, 474–477.
7. Talapin, D. V.; Lee, J.-S.; Kovalenko, M. V.; Shevchenko, E. V. Prospects of Colloidal Nanocrystals for Electronic and Optoelectronic Applications. *Chem. Rev.* **2010**, *110*, 389–458.
8. Disch, S.; Wetterskog, E.; Hermann, R. P.; Salazar-Alvarez, G.; Busch, P.; Brückel, T.; Bergström, L.; Kamali, S. Shape Induced Symmetry in Self-Assembled Mesocrystals of Iron Oxide Nanocubes. *Nano Lett.* **2011**, *11*, 1651–1656.
9. Velev, O. D. Self-Assembly of Unusual Nanoparticle Crystals. *Science* **2006**, *312*, 376–377.
10. Nykypanchuk, D.; Maye, M. M.; van der Lelie, D.; Gang, O. DNA-Guided Crystallization of Colloidal Nanoparticles. *Nature* **2008**, *451*, 549–552.
11. Park, S. Y.; Lytton-Jean, A. K. R.; Lee, B.; Weigand, S.; Schatz, G. C.; Mirkin, C. A. DNA-Programmable Nanoparticle Crystallization. *Nature* **2008**, *451*, 553–556.
12. Jones, M. R.; Macfarlane, R. J.; Lee, B.; Zhang, J.; Young, K. L.; Senesi, A. J.; Mirkin, C. A. DNA-Nanoparticle Superlattices Formed from Anisotropic Building Blocks. *Nat. Mater.* **2010**, *9*, 913–917.
13. Maye, M. M.; Kumara, M. T.; Nykypanchuk, D.; Sherman, W. B.; Gang, O. Switching Binary States of Nanoparticle Superlattices and Dimer Clusters by DNA Strands. *Nat. Nanotechnol.* **2010**, *5*, 116–120.
14. Cheng, W. L.; Dong, S.; E., W. Synthesis and Self-Assembly of Cetyltrimethylammonium Bromide-Capped Gold Nanoparticles. *Langmuir* **2003**, *19*, 9434–9439.
15. Narayanan, S.; Wang, J. Dynamical Self-Assembly of Nanocrystal Superlattices during Colloidal Droplet Evaporation by *in Situ* Small Angle X-Ray Scattering. *Phys. Rev. Lett.* **2004**, *93*, 135503.
16. Bigioni, T. P.; Lin, X.-M.; Nguyen, T. T.; Corwin, E. I.; Witten, T. A.; Jaeger, H. M. Kinetically Driven Self Assembly of Highly Ordered Nanoparticle Monolayers. *Nat. Mater.* **2006**, *5*, 265–270.
17. Smith, D. K.; Goodfellow, B.; Smilgies, D.-M.; Korgel, B. A. Self-Assembled Simple Hexagonal AB_2 Binary Nanocrystal Superlattices: SEM, GISAXS, and Defects. *J. Am. Chem. Soc.* **2009**, *131*, 3281–3290.
18. Bian, K.; Choi, J. J.; Kaushik, A.; Clancy, P.; Smilgies, D.-M.; Hanrath, T. Shape-Anisotropy Driven Symmetry Transformations in Nanocrystal Superlattice Polymorphs. *ACS Nano* **2011**, *5*, 2815–2823.
19. Choi, J. J.; Bealing, C. R.; Bian, K.; Hughes, K. J.; Zhang, W.; Smilgies, D.-M.; Hennig, R. G.; Engstrom, J. R.; Hanrath, T. Controlling Nanocrystal Superlattice Symmetry and Shape-Anisotropic Interactions through Variable Ligand Surface Coverage. *J. Am. Chem. Soc.* **2011**, *133*, 3131–3138.
20. Cheng, W. L.; Park, N.; Walter, M. T.; Hartman, M. R.; Luo, D. Nanopatterning Self-Assembled Nanoparticle Superlattices by Moulding Microdroplets. *Nat. Nanotechnol.* **2008**, *3*, 682–690.
21. Cheng, W. L.; Campolongo, M. J.; Cha, J. J.; Tan, S. J.; Umbach, C. C.; Muller, D. A.; Luo, D. Free-Standing Nanoparticle Superlattice Sheets Controlled by DNA. *Nat. Mater.* **2009**, *8*, 519–525.
22. Cheng, W. L.; Hartman, M. R.; Smilgies, D.-M.; Long, R.; Campolongo, M. J.; Li, R.; Sekar, K.; Hui, C.-Y.; Luo, D. Probing in Real Time the Soft Crystallization of DNA-Capped Nanoparticles. *Angew. Chem., Int. Ed.* **2010**, *49*, 380–384.
23. Tan, S. J.; Campolongo, M. J.; Luo, D.; Cheng, W. L. Building Plasmonic Nanostructures with DNA. *Nat. Nanotechnol.* **2011**, *6*, 268–276.
24. Martin, J. E.; Wilcoxon, J. P.; Odinek, J.; Provencio, P. Control of the Interparticle Spacing in Gold Nanoparticle Superlattices. *J. Phys. Chem. B* **2000**, *104*, 9475–9486.
25. Sastry, M.; Rao, M.; Ganesh, K. N. Electrostatic Assembly of Nanoparticles and Biomacromolecules. *Acc. Chem. Res.* **2002**, *35*, 847–855.
26. Swami, A.; Kumar, A.; Selvakannan, P. R.; Mandal, S.; Sastry, M. Langmuir-Blodgett Films of Laurylamine-Modified Hydrophobic Gold Nanoparticles Organized at the Air-Water Interface. *J. Colloid Interface Sci.* **2003**, *260*, 367–373.
27. Mogilevsky, A.; Jelinek, R. Gold Nanoparticle Self-Assembly in Two-Component Lipid Langmuir Monolayers. *Langmuir* **2011**, *27*, 1260–1268.
28. Rideal, E. K. *An Introduction to Surface Chemistry*; Cambridge University Press: Cambridge, UK, 1926.

29. Erbil, H. Y. *Surface Chemistry of Solid and Liquid Interfaces*; Blackwell Publishing Ltd., 2006.
30. Guo, X.; Ballauff, M. Spatial Dimensions of Colloidal Polyelectrolyte Brushes as Determined by Dynamic Light Scattering. *Langmuir* **2000**, *16*, 8719–8726.
31. Heitsch, A. T.; Patel, R. N.; Goodfellow, B. W.; Smilgies, D.-M.; Korgel, B. A. GISAXS Characterization of Order in Hexagonal Monolayers of FePt Nanocrystals. *J. Phys. Chem. C* **2010**, *114*, 14427–14432.
32. Förster, S.; Timmann, A.; Konrad, M.; Schellbach, C.; Meyer, A. Scattering Curves of Ordered Mesoscopic Materials. *J. Phys. Chem. B* **2005**, *109*, 1347–1360.
33. Smilgies, D.-M. Scherrer Grain-Size Analysis Adapted to Grazing-Incidence Scattering with Area Detectors. *J. Appl. Crystallogr.* **2009**, *42*, 1030–1034.
34. Dan, N.; Tirrell, M. Polymers Tethered to Curved Interfaces. A Self-Consistent-Field Analysis. *Macromolecules* **1992**, *25*, 2890–2895.
35. Xiong, H.; Sfeir, M. Y.; Gang, O. Assembly, Structure and Optical Response of Three-Dimensional Dynamically Tunable Multicomponent Superlattices. *Nano Lett.* **2010**, *10*, 3933–3939.
36. Daoud, M.; Cotton, J. P. Star Shaped Polymers: A Model for the Conformation and Its Concentration Dependence. *J. Phys. (Paris)* **1982**, *43*, 531–538.
37. Hariharan, R.; Biver, C.; Mays, J.; Russel, W. B. Ionic Strength and Curvature Effects in Flat and Highly Curved Polyelectrolyte Brushes. *Macromolecules* **1998**, *31*, 7506–7513.
38. Argillier, J.-F.; Tirrell, M. Adsorption of Water Soluble Ionic/Hydrophobic Diblock Copolymer on a Hydrophobic Surface. *Theor. Chim. Acta* **1992**, *82*, 343–350.
39. Barrat, J.-L.; Joanny, J.-F. Persistence Length of Polyelectrolyte Chains. *Europhys. Lett.* **1993**, *24*, 333–338.
40. Bai, Y.; Chu, V. B.; Lipfert, J.; Pande, V. S.; Herschlag, D.; Doniach, S. Critical Assessment of Nucleic Acid Electrostatics *via* Experimental and Computational Investigation of an Unfolded State Ensemble. *J. Am. Chem. Soc.* **2008**, *130*, 12334–12341.
41. Xiong, H.; van der Lelie, D.; Gang, O. Phase Behavior of Nanoparticles Assembled by DNA Linkers. *Phys. Rev. Lett.* **2009**, *102*, 015504.
42. Hill, H. D.; Millstone, J. E.; Banholzer, M. J.; Mirkin, C. A. The Role Radius of Curvature Plays in Thiolated Oligonucleotide Loading on Gold Nanoparticles. *ACS Nano* **2009**, *3*, 418–424.
43. Cheng, W. L.; Dong, S.; Wang, E. Site-Selective Self-Assembly of MPA-Bridged CuHCF Multilayers on APTMS-Supported Gold Colloid Electrodes. *Chem. Mater.* **2003**, *15*, 2495–2501.